A solid-state deep ultraviolet spatial heterodyne Raman system for standoff chemical detection

Rusha Chatterjee, Katharine Lunny, Michael Hilton and Jay Giblin
Physical Sciences Inc., Andover, MA 01810

ABSTRACT

There is an on-going need for sensor technologies capable of providing non-contact chemical detection and identification in the defense community. Here, we present the development of a standoff deep ultraviolet (DUV) Raman sensor for the detection of explosive residues. The sensor is based on a solid-state DUV excitation source coupled with a Spatial Heterodyne Spectrometer (SHS) receiver. The sensor is designed to detect Raman signals from a 4 cm^2 area surface at a 1 m standoff. Detection and identification is achieved by correlating measured Raman signatures with high fidelity library spectra. The DUV excitation enables operation in a solar blind spectral region, leverages ν^4 cross section scaling and resonance enhancement of Raman signatures, and minimizes the impact of sample fluorescence. The SHS receiver provides a ~1000× higher etendue than conventional slit-based spectrometers in a compact and rugged form factor, allowing for high performance field use. This work describes the system design and architecture of the Raman sensor prototype. Developmental standoff Raman measurements with the sensor using bulk liquid and solid samples are presented. Traceability to detection at the $\mu g/cm^2$ scale is demonstrated and future improvements to increase system standoff are discussed.

Keywords: Raman Spectroscopy, Spatial Heterodyne Spectrometer, Ultraviolet, Chemical Detection

1. INTRODUCTION

There has been an on-going need in the defense and security community for instruments and sensors that can detect hazardous chemical, biological, and explosive materials in the field. In this regard, Raman spectroscopy is a powerful tool due to its applicability to a wide range of targets in any state and clearly defined, sharp characteristic spectral features, unique to the material in question. However, low Raman photon intensities, limited throughputs of conventional slit spectrometers, and detrimental fluorescence backgrounds requires commercial Raman sensors to be used a few centimeters away from the interrogated surface, limiting their use in sensitive site applications.[1] Towards this end, Physical Sciences Inc. (PSI) has developed a Spatial Heterodyne Spectrometer (SHS)[2,3] based Raman sensor that operates in the deep ultraviolet (DUV) and can detect chemicals over a 4 cm^2 interrogation area from a 1 m standoff with a nominal 2 cm receiver.

PSI's Raman sensor capability combines the unique advantages of SHS spectrometers with those of DUV Raman excitation. Specifically, operation in the DUV enhances Raman signals from targets due to the λ^4 Raman cross-section scaling. Operation in a solar blind region coupled with minimal fluorescence from DUV excitation minimizes background contamination of Raman signals. The SHS Raman sensor can achieve up to ~100× higher throughputs than conventional slit spectrometers with the same spectral resolution (resolving power > 2000) with an up to ~100× lower volume.[4] The Raman DUV-SHS sensor design is modular, allowing for simple adaptation to longer standoff operation or integration with different DUV excitation lasers (233 and 262 nm demonstrated). Finally, the spectrometer has no moving parts (snapshot spectral acquisition), a compact and rugged design, and demonstrated thermal stability over a 10° C thermal cycle, making it well-suited for field use.

This work describes the design and performance of PSI's Raman sensor. Specifically, the SHS concept as well as the optical design and a radiometric model of the Raman sensor is discussed in Section 2. The sensor characterization for spectral range, resolution, modulation efficiency and thermal stability is discussed in Section 3. The capabilities of the system are demonstrated in Section 4 through Raman measurements against bulk liquids and solids.

2. SENSOR CONCEPT AND DESIGN

2.1 SHS Concept

The SHS is a snapshot version of a Fourier transform (FT) spectrometer. It of comprises a tilted Michaelson interferometer where the mirrors are replaced with fixed gratings. Unlike conventional moving mirror interferometers, the SHS generates interferograms of the input radiance in the spatial rather than temporal domain, such that all the spectral information is captured in one single snapshot.

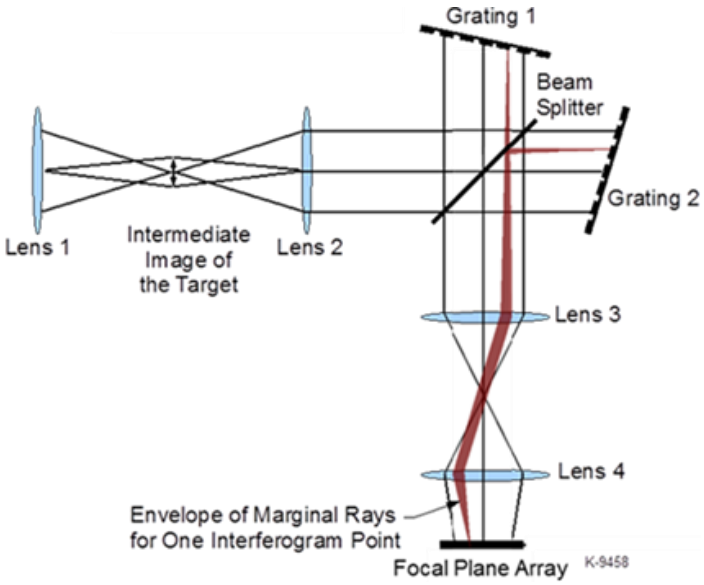

Figure 1: Schematic of SHS.

Figure 1 shows the basic SHS schematic. Radiation from the spectrometer's ground sample distance (GSD) is imaged onto the system's input aperture with Lens 1 and subsequently collimated by Lens 2. The collimated light is then split into two paths by a beamsplitter where each path is diffracted from identically ruled gratings (Grating 1 and Grating 2) mounted in a Littrow configuration. The tilted gratings introduce wavelength dependent, tilted wavefronts. Staring into the interferometer from Lens 3, tilted rays appear to diverge from the plane of the crossed gratings. Fringe optics (Lens 3 and 4) image the tilted wavefronts onto a position sensitive detector (e.g. a Charge-coupled device (CCD) image sensor) where the interfering rays produce a fringe pattern in the spatial domain (instead of the time domain in moving mirror FT spectrometers). The spatial frequencies of the fringes are proportional to the optical frequency and heterodyned about the Littrow wavelength (i.e. the gratings do not introduce a wavefront tilt at the Littrow wavelength). The spectral distribution of the GSD is extracted by taking the Fourier transform of the recorded interferogram.

2.2 Raman Receiver Optical Design

The optical layout of PSI's DUV Raman SHS is shown in Figure 2. The design includes a 2 cm refractive fore-optic that forms an image of a 22.5 mm diameter GSD (4 cm^2 area) at a 1 m standoff on the input aperture, a collimating optic that magnifies the input light onto a 300 lpmm grating (operating in the 1st diffraction order), and a pair of achromatic doublet lenses that image the resultant interference fringes onto an amplified Electron Multiplying CCD (EMCCD). The imaging arm of the SHS also includes a cylindrical lens that corrects for the inherent astigmatism of the SHS and enables high fringe contrasts (>60%) of the Raman spatial frequencies. The combination of the grating groove density, grating tilt, and magnification of the lenses[3] results in a 20 cm^{-1} spectral resolution or resolving power on the order of 2000. Performance specifications of the Raman receiver are outlined in Table 1.

Table 1: Specifications of PSI's Raman receiver.

Parameter	Value
Standoff	1 m
Receiver Diameter	2 cm
Receiver GSD	~1" diameter, ~4 cm^2
Raman Spectral Range	800 – 3000 cm^{-1}
Spectral Resolution	20 cm^{-1} (~0.1 nm)
Resolving Power	>2000

The receiver design includes the following key features:

- The system utilizes all commercial-off-the-shelf (COTS) optical components.
- The UV reflective notch filter folds the receiver optical path to enable size reduction, and additionally serves as a stray light mitigation element.
- The band pass filters provide a dual function of blocking the excitation laser wavelength and minimizing stray light and fluorescence interference.

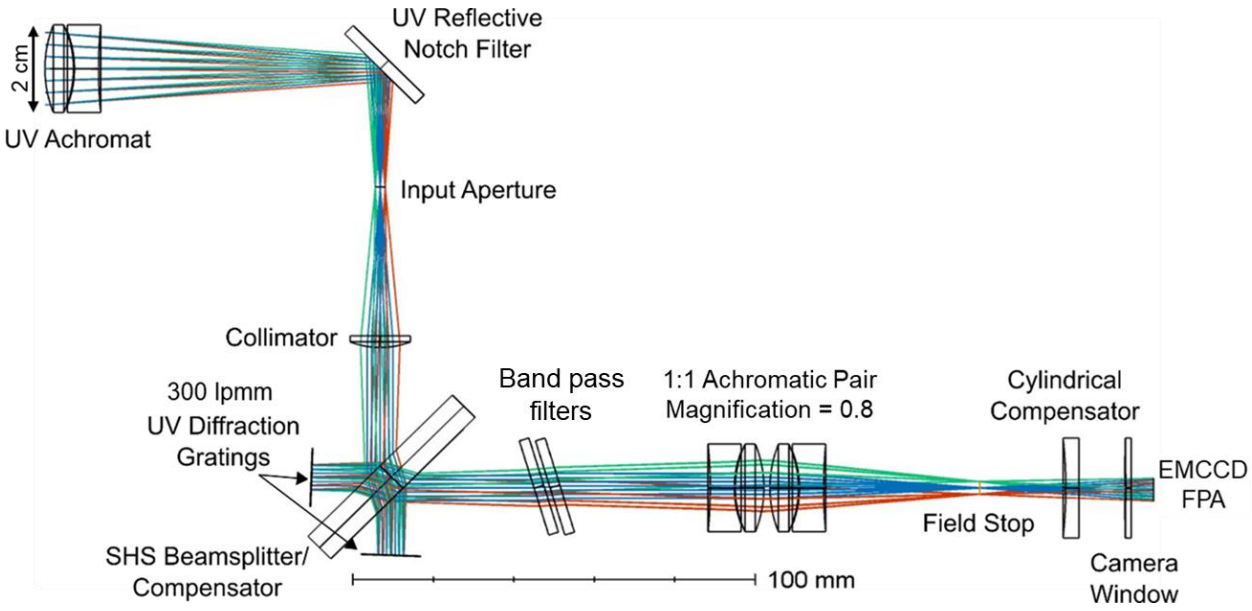

Figure 2: Optical layout of PSI's DUV Raman receiver.

Notably, the receiver design is modular with respect to the system standoff and DUV excitation used as follows:

- The optical train after the fore-optic is independent of the system standoff. As a result, the receiver design can be adapted for larger standoff operation by simply replacing the 2 cm receiver with an appropriate fore-optic. As an example, replacing the 2 cm refractive receiver optic with a ~8" diameter reflective receiver (Figure 3) enables operation at a 10 m standoff with no change to the rest of the optical design.
- The system is compatible with different DUV excitation wavelengths and simply requires the use of appropriate band pass filters and grating tilt. The receiver shown in Figure 2 has been used with both 233 and 262 nm excitation with suitable COTS filters (Semrock).

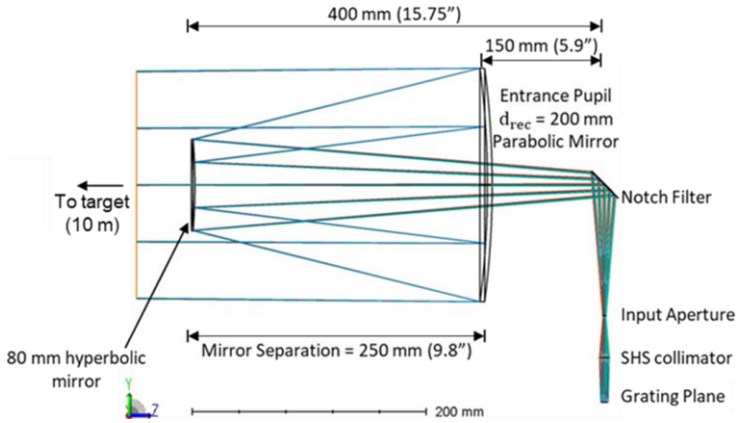

Figure 3: Example reflective receiver optic design for 10 m standoff operation.

2.3 Radiometric Performance Model

A radiometric model has been developed to predict the performance of the DUV-SHS Raman receiver and is described here. All parameters descriptions are provided in Table 2. The model predictions will be used to validate Raman measurements with the sensor against an acetonitrile standard in Section 4.

Since the SHS is a FT spectrometer, the photons from a given Raman features are dispersed into an interferogram across the number of pixels used to image the grating plane on the EMCCD. The number of Raman photons detected per pixel of the EMCCD is given by:

$$N_{Raman}(\sigma) = \frac{1}{N_{pixel,h}} * N_{mole} * \alpha_{Raman}(\sigma) * \Omega_{rec} * \eta(\sigma) * \Delta\sigma * t_{int} * \frac{I_{exc}}{hc\sigma} \int_0^d e^{-x(k_{exc}+k_\sigma)} dx. \quad (1)$$

Here, the term in the integral explicitly accounts for excitation, as well as scattered Raman photon losses through the volume of the interrogated sample. For materials like acetonitrile the integral is ~1. However, for materials which have a measurable DUV absorption, this factor becomes significant, as shown in Section 4.

The noise in the measurement arises from the inherent detector noise and photon shot noise. The detector noise (readout, dark and spurious) expressions are well established in the literature on EMCCDs and will not be reproduced here.[5] The per-pixel shot noise in the SHS arises from two sources – the full Raman spectrum (N_{full}) and excitation bleedthrough through the system (N_{exc}). These can be calculated as follows:

$$N_{full} = \int_{\sigma_{min}}^{\sigma_{max}} N_{Raman}(\sigma)\, d\sigma, \text{ and} \tag{2}$$

$$N_{exc} = \frac{1}{N_{pixel,h}} * \frac{P_{Laser}}{2\pi * hc\sigma_{exc}} * R_{surface}(\sigma_{exc}) * \Omega_{rec} * \eta(\sigma_{exc}) * t_{int}. \tag{3}$$

The total shot noise per pixel shot noise is therefore:

$$\delta_{shot} = F * M * \sqrt{QE * \left(N_{full} + N_{exc}\right)}. \tag{4}$$

The signal-to-noise ratio (SNR) for a given Raman feature in spectral space (i.e. after a FT) is therefore:

$$SNR(\sigma) = \frac{N_{pixel,h} * M * ME * QE * N_{Raman}(\sigma)}{\sqrt{N_{pixel,h}(\delta_{det}^2 + \delta_{shot}^2)}} \tag{5}$$

The expression takes into account that during a FT, all the energy for a given spatial frequency dispersed in the interferogram is put back into the peak. The peak intensity is impacted by the interferogram fringe contrast or modulation efficiency (ME). Additionally, since the shot noise is also dispersed across all the pixels, the FT adds the noise from all pixels into the peak intensity. Based on expressions 1 – 6, projections can be generated for the system performance against explosives. For example, using known absorptivity and cross-section values of ammonium nitrate,[6] model predictions indicate that DUV Raman sensor can detect the discriminant 1041 cm^{-1} Raman feature from a 10 μm thin film (equivalent to an areal density of ~1.7 mg/cm^2) with an SNR of 5 in 10 min using 262 nm excitation. Calculations assume 50 mW power at the sample dispersed over a ~400 mm^2 area (2.25 cm diameter).

Table 2: Radiometric model parameter description.

Parameter	Description	Units
σ	Raman wavenumber	cm^{-1}
σ_{exc}	Excitation laser wavenumber	cm^{-1}
σ_{min}	Lower end of Raman spectral range	cm^{-1}
σ_{max}	Upper end of Raman spectral range	cm^{-1}
$N_{Raman}(\sigma)$	Number of Raman photons detected for σ	photons
N_{mole}	No. of molecules in sample volume	mole
$\alpha_{Raman}(\sigma)$	Raman cross section at σ	$cm^2\ sr^{-1}\ mole^{-1}\ cm^{-1}$
Ω_{rec}	Receiver collection solid angle	sr
$\eta(\sigma)$	Receiver transmission efficiency at σ	-
$\Delta\sigma$	Spectral bandwidth of receiver	cm^{-1}
t_{int}	Integration time	s
I_{exc}	Excitation intensity at receiver GSD	$W\ cm^{-2}$
P_{exc}	Excitation power at receiver GSD	W
d	Thickness of sample	cm
k_{exc}	Sample attenuation coefficient at excitation wavelength	cm^{-1}
k_{σ}	Sample attenuation coefficient at Raman wavelength	cm^{-1}

Parameter	Description	Units
$N_{pixel,h}$	Number of interferogram sampling pixels	-
$R_{surface}(\sigma_{exc})$	Surface reflectance at $\boldsymbol{\sigma_{exc}}$	-
M	EMCCD gain	-
F	EMCCD amplification noise factor	-
QE	EMCCD quantum efficiency	photoelectrons/photon
δ_{shot}	Per pixel shot noise	photoelectrons
δ_{det}	Per pixel total detector noise	photoelectrons
ME	Interferogram modulation efficiency	-

3. SENSOR PROTOTYPE AND CHARACTERIZATION

3.1 Prototype Sensor Assembly

A representative example of PSI's Raman prototype sensor is shown in Figure 4. Specifically, Figure 4a shows the receiver integrated with a 233 nm DUV excitation source (Science and Engineering Services) into a single common chassis. The system has a bistatic transmitter/receiver design with the excitation spot overlapping with the receiver's GSD at a 1 m standoff. Scattered Raman photons from the surface are collected in a backscattering geometry. Figure 4b shows a photograph of the exterior of the sensor. The sensor is equipped with a range finder and context camera and has an overall size of 9.75 × 9.5 × 18.75 in^3 (driven by the size of the EMCCD and DUV laser). Figure 4c shows the DUV excitation spot at the receiver's GSD. The excitation spot (240 mm^2 area) under-fills the receiver GSD (400 mm^2) in this case due to the shape and divergence of the DUV laser output.

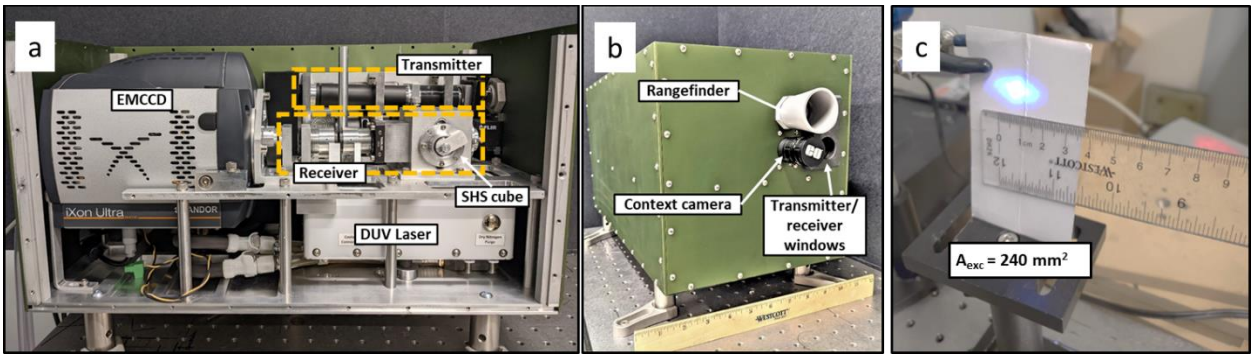

Figure 4: Representative example of PSI's prototype Raman sensor. (a) Sensor interior showing the SHS receiver integrated with a 233 nm DUV laser into a common chassis. (b) Sensor exterior. (c) DUV excitation spot at the sensor's GSD.

3.2 DUV Interferograms and Spectral Resolution

The DUV-SHS Raman receiver performance was characterized with the 253.6 nm line from a mercury (Hg) pen lamp placed at the receiver's GSD, 1 m from the receiver, as shown in Figure 5. Figure 6 shows an example of a representative measurement with the DUV-SHS receiver. Specifically, Figure 6a shows the image of the SHS grating plane (pupil) acquired with the EMCCD. Clear fringes associated with the 253.6 nm line are apparent in the image.

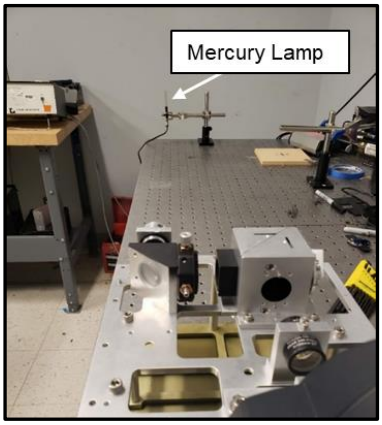

Figure 5: Example set-up of Hg lamp relative to prototype receiver.

Figure 6b plots the line profile of the image (extracted from a 6-pixel wide region shown by the dashed red box). The interferogram has a fringe contrast of 74% demonstrating the ability of the SHS to generate high quality interferograms. In this regard, the fringe contrast in an interferogram is directly proportional to the strength of the signal observed in the associated FT. Figure 6c shows the associated FT (solid blue line) of the interferogram in Figure 6b where a clear peak associated with the spatial frequency of the

interferogram (9.8 lpmm) is visible. The dashed black line shows a Gaussian fit to the peak. The width of the Gaussian, coupled with a wavelength calibration of the fringe axis using the known Hg wavelength (data not shown) indicates a ~19 cm^{-1} spectral resolution of the SHS receiver.

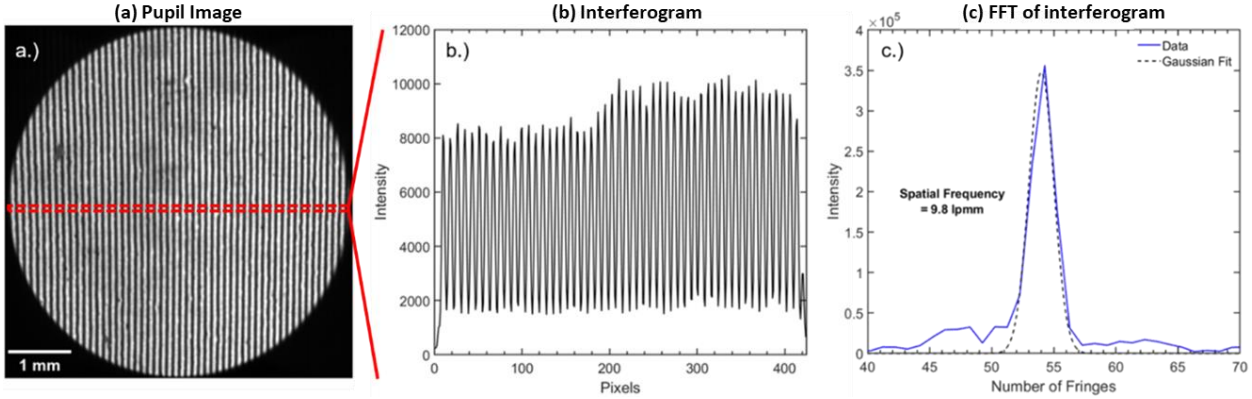

Figure 6: (a) Pupil image, (b) extracted line profile and (c) resultant FFT of the Hg 253.6 nm line acquired by the DUV-SHS receiver.

3.3 Modulation Efficiency

The Hg lamp was also used to characterize the fringe contrast of DUV interferograms as a function of spatial frequency to evaluate the receiver's ability to image spectral features across the Raman spectral range (where the spatial frequency is directly related to wavelength). This was done by varying the tilt of the SHS gratings to adjust the Littrow configuration and generate 253.6 nm interferograms across a range of spatial frequencies. Since Raman measurements require collecting photons from the full field, the pupil images were summed in the vertical direction to extract a full-field interferogram and were subsequently used to calculate interferogram modulation efficiency (ME) or fringe contrast as:

$$ME = \frac{I_{max} - I_{min}}{I_{max} + I_{min}}, \tag{6}$$

where I_{max} (I_{min}) are the peak (valley) intensities of the interferogram fringe. An example of the calculation of the ME is shown in Figure 7. Specifically Figure 7a shows the pupil image of the Hg 253.6 nm line at 7.2 lpmm. Figure 7b shows the resultant interferogram and I_{max} and I_{min} values used to calculate ME.

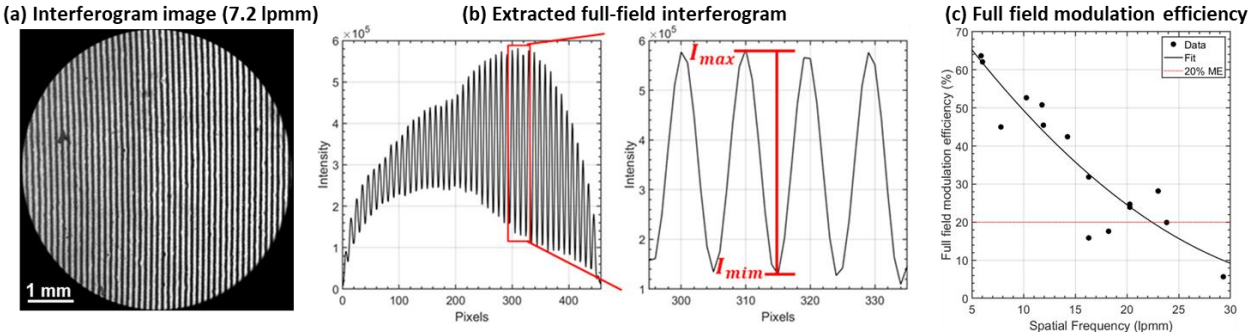

Figure 7: (a) Hg interferogram image at 7.2 lpmm. (b) Extracted interferogram by summing (a) along the vertical axis. (c) Measured Hg interferogram ME as a function of spatial frequency (solid black circles). The solid black line is a fit to the data points and serves as a guide to the eye.

Figure 7c plots the measured ME (solid black circles) as a function of interferogram spatial frequency. The ME values here are generally lower than associated on-axis fringe contrast values. This arises from slight vertical tilt in the fringes along the vertical direction (due to slight vertical tilt in gratings) and well a small irregularities along the vertical axis (due to grating wavefront errors), which reduce the overall ME of the full-field interferogram. The vertical tilt in the interferogram also causes the scatter in the measured ME values.

Figure 7c also shows a best fit curve to the ME data points (solid black curve). This curve serves as a guide to the eye to determine the resolution limit of the SHS receiver. In this regard, we consider the Rayleigh criteria of 20% contrast (horizontal dashed red line) as the limiting value. Based on this criteria, the SHS receiver can clearly resolve interferograms with spatial frequencies up to 22 lpmm.

3.4 Thermal Stability

A quantitative evaluation of the impact of temperature changes on the DUV-SHS was characterized by attaching two polyamide heaters to the interferometer cube. This was done on an older iteration of the Raman sensor, but with the same mechanical design of the SHS cube. Figure 8a shows a picture indicating the placement of the heaters and thermocouples on the SHS cube. The heaters achieved a maximum power output of 8.4 W. The associated changing temperature profile is plotted in Figure 8b. The plot shows that the heaters achieved a temperature cycling over ~10 °C (~20.5 – 30.5 °C). A series of interferograms were acquired from the Hg 253.65 nm line as a function of temperature.

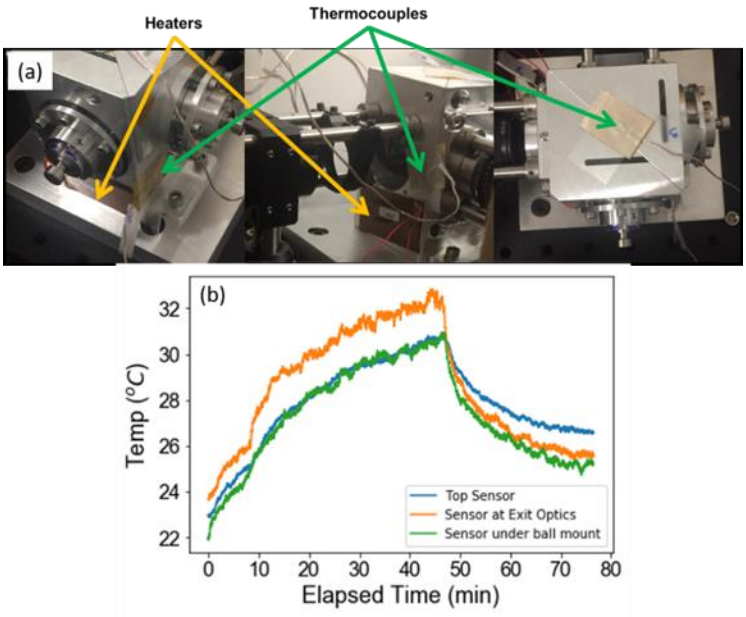

Figure 8: (a) Positions of heaters and thermocouples on the interferometer cube. (b) Temperature cycling profile achieved with the heaters.

Figure 9a plots the measured number of Hg interferogram fringes (or FT peak position) for each temperature during the heating and cooling temperature cycle. The asymmetric change in the fringe number indicates a hysteresis in the mechanical changes in the cube during the temperature cycling. Overall, a change of 4 fringes was seen over the 10 °C cycle corresponding to a tilt change of 50 µrad (5 µrad/°C) and a 40 cm^{-1} of apparent spectral shift. Notably, no change was observed in the resolving power of the cube. In addition, a tilt change was only observed along the horizontal direction, not vertical, as indicated by the unchanged ME across the temperature cycle, plotted in Figure 9b. These results indicates that the DUV-SHS Raman receiver does not require any active alignment to maintain performance but only a wavelength calibration with a Hg pen lamp in the event of a temperature change.

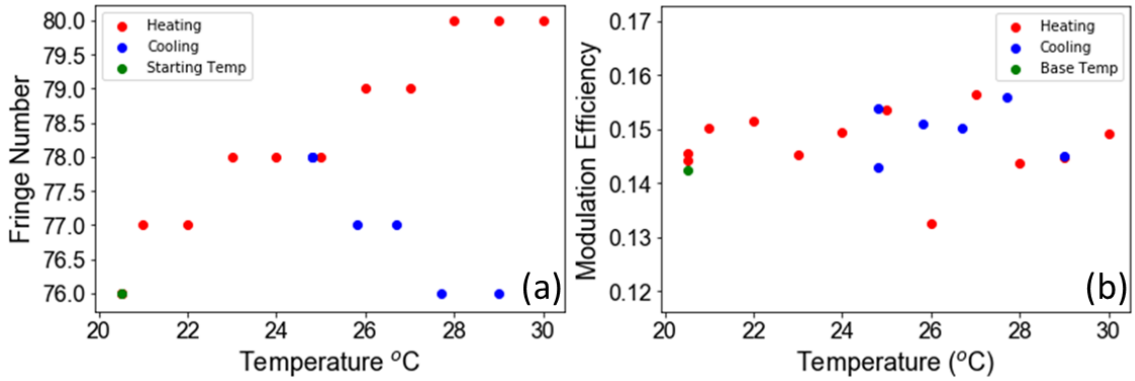

Figure 9: Observed number of (a) Hg fringes and (b) interferogram ME as a function of temperature.

4. RAMAN MEASUREMENTS

4.1 Performance validation: Acetonitrile

Raman measurements on bulk acetonitrile were performed with 233 nm excitation using the prototype DUV-SHS Raman sensor by placing a DUV transparent cuvette of acetonitrile at the sensor's GSD. The measurement set-up is illustrated in Figure 10. Since the acetonitrile Raman cross-section is well characterized in the literature (C–H stretch cross-section at 233 nm excitation: 15×10^{-29} $cm^2mol^{-1}sr^{-1}$),[7] these measurements were also used to validate the performance of the DUV-SHS receiver based on the radiometric model (Section 2.3).

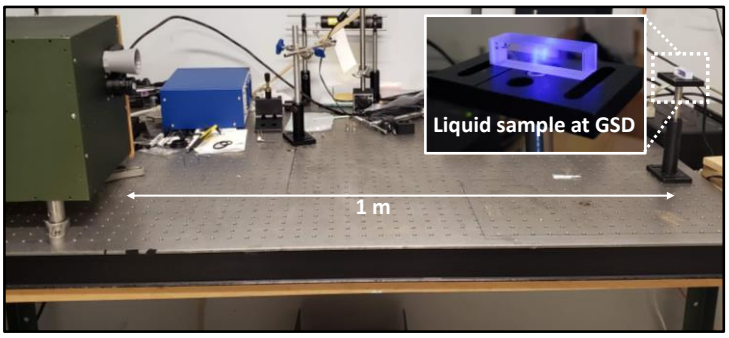

Figure 10: Raman measurement configuration with acetonitrile.

Figure 11 shows the measured (solid blue) and model predicted (dashed black) Raman (a) interferogram and associated (b) spectrum, acquired from a cuvette of acetonitrile. Measurement parameters are as follow:

- Area of excitation spot at the GSD: 240 mm^2
- Excitation wavelength: 233 nm
- SHS Littrow: 1700 cm^{-1}
- Excitation power at GSD: 3.5 mW
- Cuvette path length: 1 cm
- Integration time: 4s

Two clear peaks are observed in the spectrum and are associated with the acetonitrile 2250 cm^{-1} C≡N and 2940 cm^{-1} C–H stretches, demonstrating the sensor's ability to generate high fidelity Raman spectra.

Table 3 lists the comparison of observed and model predicted interferogram counts and SNR. In this regard, interferogram counts represent the signal alone, while the SNR additionally factors in the noise. The observed interferogram counts are within a factor of 2 with associated measured values, demonstrating that that the system model can capture the expected Raman signal with reasonable accuracy. The SNR was measured in spectral space for the 2940 cm^{-1} CH stretch and defined as the ratio of peak intensity to the standard deviation in the baseline, as shown in Figure 11b. Observed and expected values are in close agreement with each other. This suggests that the model is slightly overestimating the observed noise in the system. However, the measurements with acetonitrile confirm that the prototype Raman system is performing as expected, in accordance with the radiometric model predictions.

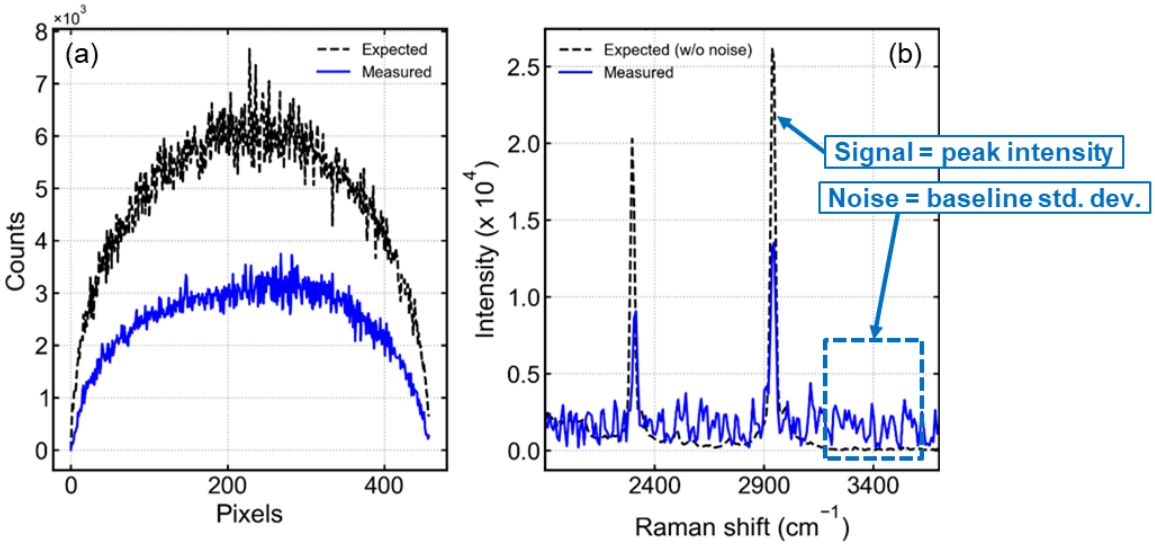

Figure 11: Measured (solid blue) and model predicted (dashed black) (a) interferograms and (b) associated Raman spectra of acetonitrile acquired in backscattering configuration.

Table 3: Comparison of observed and model predicted interferogram counts and SNR.

Metric	Observed	Model	Observed/Model
Median interferogram counts	2675.0	5273.4	0.5
Spectral SNR	19.3	15.4	1.3

4.2 Measurements with bulk solids

Raman measurements with bulk solids were performed by packing solids into a 1" diameter bottle cap and mounting the sample at the sensor's GSD as shown in Figure 12. Measurements were conducted with a 262 nm excitation source (CrystaLaser) which formed a 260 mm^2 excitation spot at the GSD with 26 mW total power. The SHS gratings were set to Littrow at 700 cm^{-1} Raman shift.

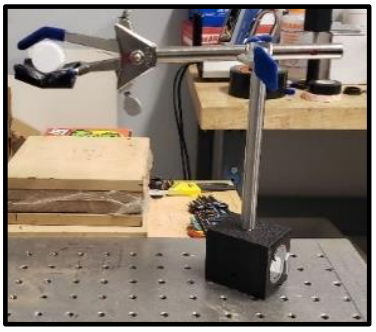

Figure 12: Solid sample mounting configuration at the sensor's GSD.

Figure 13 shows the measured (a) interferogram and (b) associated extracted Raman spectrum (solid blue), acquired with a 9 s integration. A reference Raman spectrum (dotted red) is also overlaid with the measured spectrum.[8] The measured and reference spectra in Figure 13b are in good agreement. Specifically, both the strong 1012 cm^{-1} feature as well as higher frequency, lower intensity features are reproduced in the measured Raman spectrum. This further demonstrates the ability of the Raman sensor to generate high fidelity Raman spectra which can be subsequently used for detection.

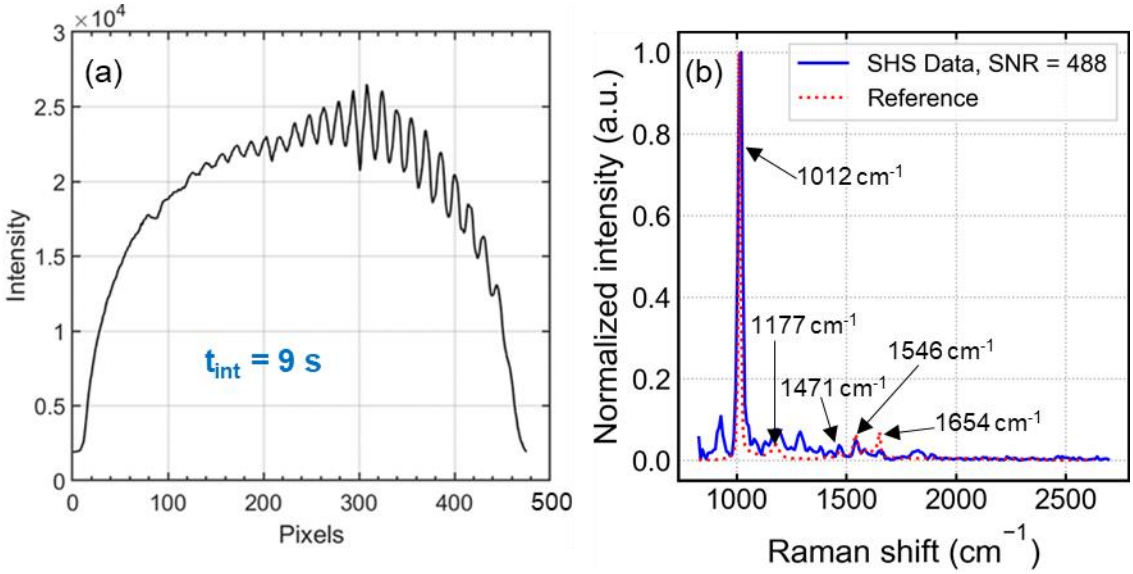

Figure 13: (a) Measured interferogram of bulk urea in 9 s. (b) Associated measured Raman spectrum (solid blue) overlaid with a literature reference (dotted red). SNR reported is for the strongest Raman feature.

Figure 14 shows measured Raman spectra (solid blue lines) of bulk (a) sodium sulfate, (b) potassium chlorate and (c) ammonium nitrate. All spectra were acquired with a 45 s integration time with 26 mW of excitation power at the sample. Also overlaid in the plots are associated reference spectra (dotted red) for each solid.[9,10] It can be seen that the sensor generates high SNR spectra for each solid. The discriminant feature of each solid in the 950-1050 cm^{-1} spectral range, as well as the lower intensity Raman features are clearly reproduced in the measured spectra.

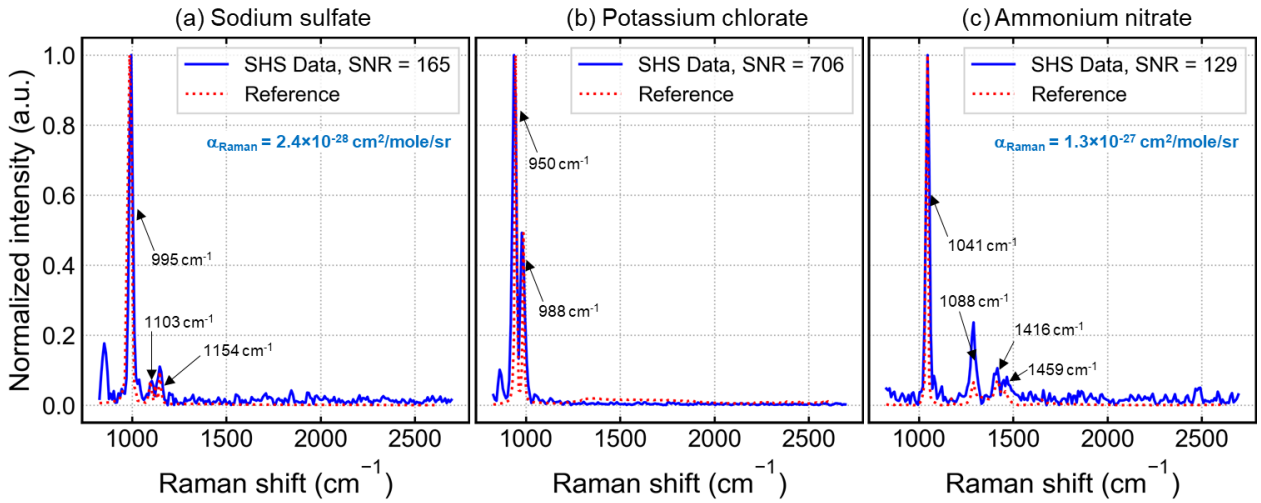

Figure 14: Measured (solid blue) and associated reference (dotted red) Raman spectra of bulk (a) sodium sulfate, (b) potassium chlorate and (c) ammonium nitrate. Reported SNRs are for the strongest Raman features. Integration time of 45 s used for all acquisitions.

Notably, the ammonium nitrate spectrum has a lower SNR than that of sodium sulfate despite the ~5× higher Raman cross-section.[6,7] This is due to the loss of excitation and scattered Raman photons from absorbance through the bulk of the solid. In this regard, ammonium nitrate has a reported measurable absorption the excitation and Raman wavelengths of these measurements[6] while sodium sulfate (to the best of our knowledge from a literature survey) does not. This effect is verified by using the sensor's radiometric model to generate SNR predictions of a 1 cm thick layer of the solid. The model factors in reported absorptivity values of ammonium nitrate and assumes no DUV absorption of sodium sulfate. Model calculations show that SNRs of ~153 and ~38 (in 45 s with 26 mW of excitation power) can be expected in the sensor-acquired spectra. While the 1 cm thick layer does not exactly represent the samples used in Figure 12, model predictions reproduce the experimental trends in SNRs, verifying the impact of absorption. These trends are additionally in agreement with literature reports of resonance Raman measurements of bulk ammonium nitrate where the DUV cross-section enhancement effect is counteracted by the lower DUV penetration depths in bulk measurements.[6]

5. CONCLUSIONS

In conclusion, the work presented here demonstrates the capabilities of PSI's DUV-SHS standoff Raman sensor. The senor combines the advantages of high SHS throughput and λ^4 Raman cross-section scaling in DUV wavelengths. A nominal 2 cm receiver allows interrogation of a ~1" diameter area (roughly the area of a thumbprint) from a 1 m standoff. The DUV-SHS receiver has a modular design and allows operation with different excitation wavelengths (through use of appropriate band pass filters) and standoffs (by interchanging the fore-optic). The SHS cube has a robust design that maintains the spectrometer's resolving power (>2000) over a 10° C thermal cycle and generates high quality clearly resolvable DUV interferograms with ≥20% fringe contrast for spatial frequencies up to 22 lpmm. The sensor generates high fidelity Raman spectra of bulk solids and liquids with validated system performance against known standards. The system is therefore well suited for detection and identification of chemicals and explosives in sensitive sites where contact with the sample is unsafe or not feasible.

ACKNOWLEDGEMENT OF SUPPORT AND DISCLAIMER

This material is based upon work supported by USA CONTRACTING CMD-APG. - W911SR under Contract Number W911SR-20-C-0003 and W911SR-18-C-0037. Any opinions, findings and conclusions or recommendations expressed in this material are those of the author(s) and do not necessarily reflect the views of USA CONTRACTING CMD-APG. - W911SR.

REFERENCES

[1] Moore, D.S., “Instrumentation for trace detection of high explosives,” Rev. Sci. Instrum., 75, 2499 –2512 (2004).
[2] Harlander, J., Reynolds, R.J., and Roesler, F.L., “Spatial heterodyne spectroscopy for the exploration of diffuse interstellar emission lines at far-ultraviolet wavelengths”, Astrophys. J., 396, 730-740 (1992).
[3] Harlander, J.M., “Spatial heterodyne spectroscopy: Interferometric performance at any wavelength without scanning”, Ph.D. Dissertation, Univ. Wisconsin-Madison (1991).
[4] Ciaffoni, L., Matousek, P., Parker, W., McCormack, E.A. and Mortimer H., “Grating spectrometry and spatial heterodyne Fourier transform spectrometry: Comparative noise analysis for Raman measurements”, Appl. Spectrosc., 75, 241–249 (2021).
[5] Dussault, D. and Hoess, P., "Noise performance comparison of ICCD with CCD and EMCCD cameras", Proc. SPIE, 5563 (2004).
[6] Emmons, E.D., Tripathi, A., Guicheteau, J.A., Fountain, A.W. and Christensen, S.D., “Ultraviolet resonance Raman spectroscopy of explosives in solution and the solid state”, J. Phys. Chem. A, 117, 4158−4166 (2013).
[7] Dudik, J.M., Johnson, C.R., and Asher, S.A., “Wavelength dependence of the preresonance Raman cross sections of CH_3CN, SO_4^{2-}, ClO_4^-, and NO_3^-”, J. Chem. Phys., 82, 1732 (1985).
[8] AIST spectral database, https://sdbs.db.aist.go.jp/sdbs/cgi-bin/cre_index.cgi
[9] Lamsal, N., and Angel, S.M., “Deep-ultraviolet Raman measurements using a spatial heterodyne Raman spectrometer (SHRS)”, Appl. Spec., 69, 5, 525-534 (2015).
[10] Explosives Database, Univ. of Rhode Island, http://expdb.chm.uri.edu